Enhanced localized dipole of Pt-Au single-site catalyst for solar water splitting

Xingyu Liu[a], Zhifei Hao[a], Haitao Wang[a], Tuo Wang[b], Zhurui Shen[a,c,1], Hao Zhang[c], Sihui Zhan[a,1], and Jinlong Gong[b,d,1]

[a]Ministry of Education Key Laboratory of Pollution Processes and Environmental Criteria Tianjin Key Laboratory of Environmental Remediation and Pollution Control, College of Environmental Science and Engineering, Nankai University, Tianjin 300350, China; [b]Key Laboratory for Green Chemical Technology of Ministry of Education, School of Chemical Engineering and Technology, Tianjin University, Tianjin 300072, China; [c]School of Materials Science and Engineering, Nankai University, Tianjin 300350, China; and [d]Joint School of National University of Singapore and Tianjin University, International Campus of Tianjin University, Binhai New City, Fuzhou 350207, China

Edited by Alexis Bell, Department of Chemical and Biomolecular Engineering, University of California, Berkeley, CA; received October 28, 2021; accepted January 5, 2022

Solar water splitting is regarded as holding great potential for clean fuels production. However, the efficiency of charge separation/transfer of photocatalysts is still too low for industrial application. This paper describes the synthesis of a Pt-Au binary single-site loaded g-C_3N_4 nanosheet photocatalyst inspired by the concept of the dipole. The existent larger charge imbalance greatly enhanced the localized molecular dipoles over adjacent Pt-Au sites in contrast to the unary counterparts. The superposition of molecular dipoles then further strengthened the internal electric field and thus promoted the charge transportation dynamics. In the modeling photocatalytic hydrogen evolution, the optimal Pt-Au binary site photocatalysts (0.25% loading) showed 4.9- and 2.3-fold enhancement of performance compared with their Pt and Au single-site counterparts, respectively. In addition, the reaction barrier over the Pt-Au binary sites was lowered, promoting the hydrogen evolution process. This work offers a valuable strategy for improving photocatalytic charge transportation dynamics by constructing polynary single sites.

solar water splitting | binary single sites | localized dipole | internal electric field

Solar water splitting has attracted worldwide attention due to its immense potential in clean fuel production. It is roughly composed of two processes: photogenerated charge separation/transfer and surface chemical reactions. The photogenerated charge separation and transfer is widely regarded as the rate-limiting step, and its low efficiency is the crucial challenge that needs to be addressed (1–3). Therefore, much effort has been devoted to developing new strategies in surface/interface engineering of photocatalysts to improve the dynamics of charge separation/transportation, and the key is to construct effective built-in electric fields or even tune the diffusion process of charges (1, 3, 4).

Recently, single-atom or single-site catalysts (SACs) sparked considerable research interest in photocatalysis and many other heterogeneous catalytic processes (5–9). Generally, due to their unique electronic and geometric structures, single metal sites can improve the photocatalytic performance mainly by optimizing the charge evolved surface chemical reactions (e.g., the adsorption of reactants or charge transfer from catalysts to reactants) (10, 11). However, single metal sites do not obviously change the charge transportation process of the photocatalyst and thus hardly contribute to the enhancement of charge separation and transfer, which greatly limits the promotion of SACs for particulate photocatalysis. Inspired by the synergy between metal species in classical catalytic reactions, very recently, binary metal site catalysts have been developed to achieve the promotional effect of binary atomic sites, and a few successful cases have been investigated (12–14). However, it is still a challenge to construct effective binary sites.

It is known that the dipole with one positive center and one negative center is the basic unit of electric fields, which are the main driving force of charge separation and transfer. Enlightened by this concept, we have designed and constructed a Pt-Au binary single-site loaded g-C_3N_4 nanosheet photocatalyst (Pt-Au SAC), which resulted in enhanced localized molecular dipoles in the zone of adjacent Pt-Au sites due to their larger charge imbalance compared with those in unary counterparts. Therefore, via the superposition of these enhanced molecular dipoles, the internal electric field was effectively strengthened for Pt-Au SAC, which is stronger than those of Pt and Au single-site counterparts. As confirmed by multiple spectroscopic methods, including femtosecond transient absorption spectroscopy (TA), the stronger internal electric field of Pt-Au SAC can significantly enhance the charge transportation dynamics. As a result, in solar water splitting, the hydrogen evolution rate of optimum Pt-Au SAC (0.25% metal loading) was boosted to 1.88 mmol g^{-1} h^{-1} (apparent quantum efficiency 1.72% at 365 nm), 4.9 and 2.3 times over Pt and Au single-site counterparts (Pt SAC and Au SAC, respectively). Besides, a lower energy barrier was also realized over the Pt-Au binary sites, further stimulating its catalytic performance. Previously, several

Significance

Single-atom or single-site catalysts have received considerable research interest in photocatalysis and many other heterogeneous catalytic processes. However, the single metal sites did not obviously change the charge transportation process of the photocatalyst and thus hardly contributed to the enhancement of charge separation and transfer. Inspired by the synergy between metal species in classical catalytic reactions, this research presents a strategy of constructing a Pt-Au binary single-site catalyst. Pt-Au binary single sites not only functioned as the catalytic reactive sites but also modulated the charge distribution and enhanced the internal electric field. The concept and the strategy of this work are expected to provide a novel perspective for improving photocatalytic charge transportation dynamics.

Author contributions: X.L., Z.S., S.Z., and J.G. designed research; X.L. performed research; X.L., Z.H., H.W., T.W., Z.S., H.Z., S.Z., and J.G. analyzed data; and X.L., Z.S., S.Z., and J.G. wrote the paper.

The authors declare no competing interest.

This article is a PNAS Direct Submission.

[1]To whom correspondence may be addressed. Email: shenzhurui@nankai.edu.cn, sihuizhan@nankai.edu.cn, or jlgong@tju.edu.cn.

This article contains supporting information online at http://www.pnas.org/lookup/suppl/doi:10.1073/pnas.2119723119/-/DCSupplemental.

Published February 14, 2022.

reports about other binary single sites catalysts have shown their advances as the synergistic reaction centers for optimizing the reaction barriers or rate-determining steps (12–14). In our case, the Pt-Au binary sites not only contribute to the lower reaction barriers but also finely contribute to charge transportation dynamics by enhancing the localized molecular dipoles. This discovery offered a strategy for improving the surface charge separation/transfer of photocatalysis, which is one of the central problems for improving the photocatalytic process.

Results

Identification of Pt-Au Binary Single Sites. The as-prepared single-site catalysts 0.25% Pt SAC, 0.25% Au SAC and binary sites catalyst 0.25% Pt-Au SAC were firstly subjected for microstructure analysis (Fig. 1). Elemental mappings exhibited that Pt and Au were homogeneously distributed on the g-C_3N_4 substrate (Fig. 1*D*, *SI Appendix*, Figs. S1 and S2). The loading contents of Pt and Au were determined by inductively coupled plasma mass spectrometry (ICP-MS) (*SI Appendix*, Table S1). High-angle annular dark-field scanning transmission electron microscopy (HAADF-STEM) was then employed to confirm the state of the metal elements, and the bright spots in Fig. 1*B* show that Pt and Au are single atoms (also shown in *SI Appendix*, Figs. S3 and S4). This was further confirmed by the selected area intensity surface plot for a pair of isolated atoms (Fig. 1 *E* and *F*). The atomic distances between adjacent isolated atoms were counted (Fig. 1*C*), which showed that the predominant atomic distances were in the range of 0.4–0.7 nm. The distance between two adjacent metal atoms (where the area is labeled "a" as shown in Fig. 1 *B* and *E*) was 0.694 nm, which is close to the theoretical distance between two adjacent metal atoms located in two heptazine cavities (Fig. 1*F*). Besides, X-ray powder diffraction (XRD) patterns, Fourier transform infrared spectra, thermal analysis, elemental analysis, Brunauer–Emmett–Teller measurement, and related pore analysis indicated that other physical and chemical characteristics of Pt, Au, and Pt-Au SACs are almost identical (*SI Appendix*, Figs. S5–S7 and Tables S2 and S3).

Generally, the performance of SACs largely depended on the coordination structure of single centers, thus the precise structural analysis using multiple spectroscopic and theoretical simulations was performed (Fig. 2 and *SI Appendix*, Fig. S8). As shown in X-ray absorption near-edge structure spectrum of Pt L_3-edge, 0.25% Pt-Au SAC and 0.25% Pt SAC exhibited higher white line intensities than Pt foil, which is a typical feature of SACs (*SI Appendix*, Fig. S8*A*) (14). The white line intensities of 0.25% Pt-Au SAC and 0.25% Au SAC were also higher than Au foil, as shown in Au L_3-edge spectrum (*SI Appendix*, Fig. S8*B*). Those results were consistent with the HAADF-STEM observations, revealing the atomic nature of metal species. The extended X-ray absorption fine structure (EXAFS) spectra showed main peaks of as-prepared SACs between 1 and 2 Å (Pt/Au-N coordination), apparently different from the metal bonding peaks in Pt and Au foils, and no new peaks were observed, indicating the absence of Pt-Au bond. The fitting results of EXAFS also indicated the absence of metal bonds like Pt-Pt, Pt-Au, and Au-Au, confirming the atomic dispersion of Pt and Au (*SI Appendix*, Fig. S9 and Table S4), which was

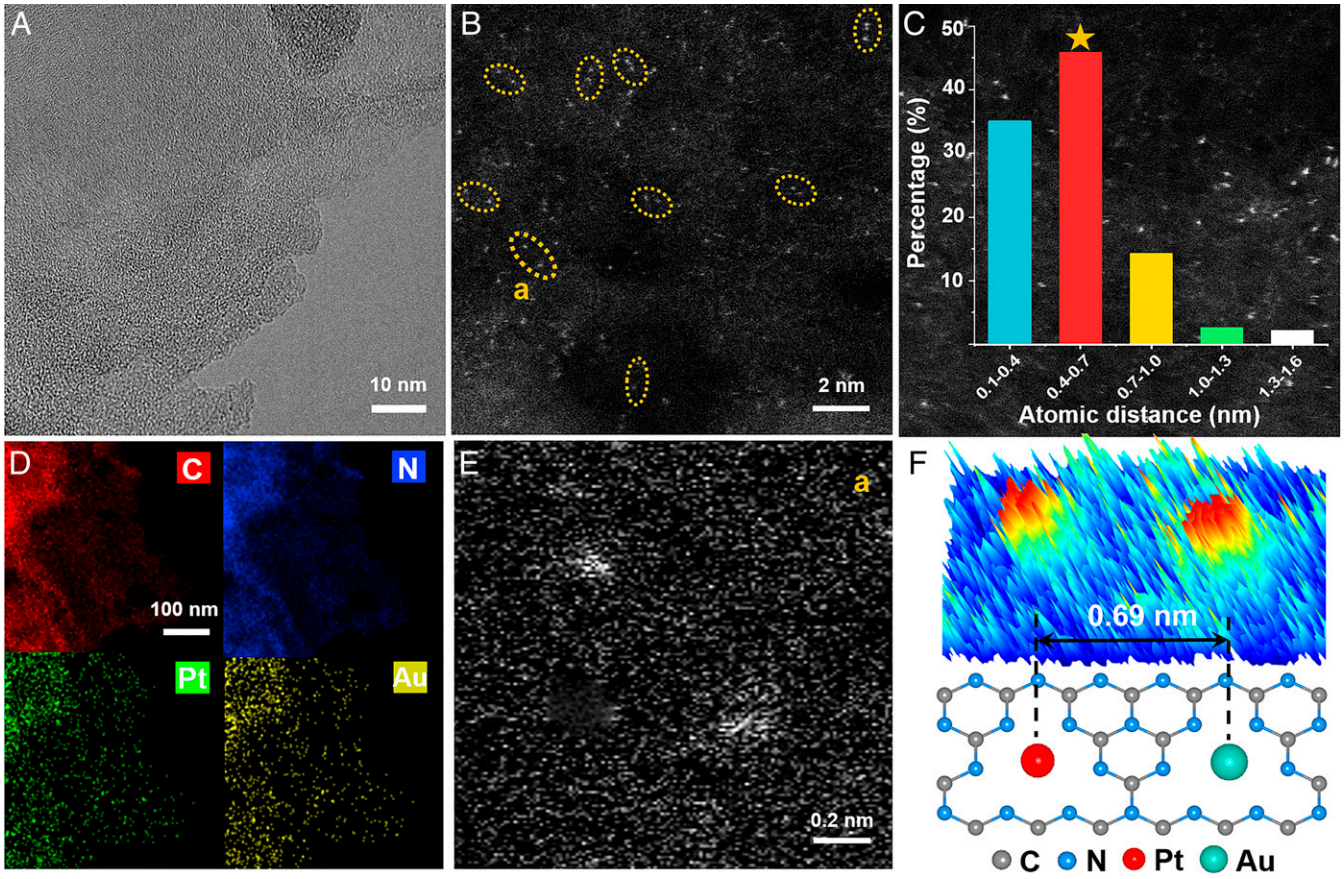

Fig. 1. Observation of Pt-Au binary single sites at atomic level. (*A* and *B*) A HR-TEM image and a HAADF-STEM image of Pt-Au SAC. (*C*) Atomic distance statistics based on multiple HAADF-STEM images. (*D*) Elemental mappings of Pt-Au SAC. (*E*) Magnified binary atomic pair as circled in the HAADF-STEM image of (*B*) (where the area is labeled "a"). (*F*) Corresponding intensity surface plot of the selected atomic pair (*E*) and theoretical model of g-C_3N_4 with two metal atoms located in the adjacent sixfold cavities.

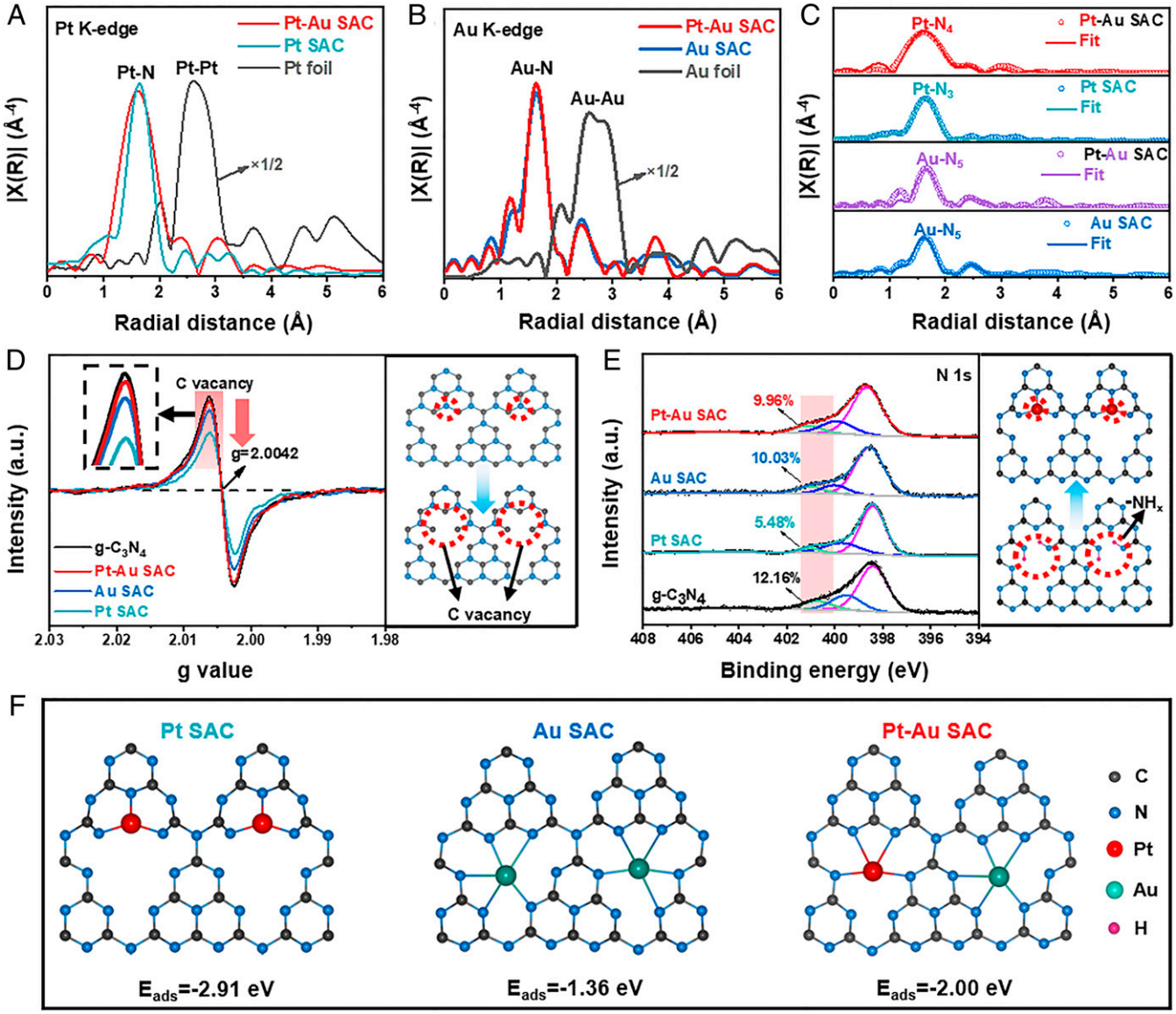

Fig. 2. Identification of the chemical structure of Pt-Au binary single sites. (*A* and *B*) Fourier transforms of EXAFS spectra (Pt K-edge and Au K-edge) at R space. (*C*) EXAFS fitting curves of as-prepared SACs. (*D*) EPR spectra of different samples and corresponding diagram of C vacancy. (*E*) N 1s XPS of different samples and corresponding illustration of -NH_x. (*F*) Precise coordination structures determined by spectroscopic analysis and DFT optimization.

also evidenced by the wavelet transform analysis (Fig. 2*C* and *SI Appendix*, Fig. S10). Moreover, the coordination parameters extracted from the fitting curves (*SI Appendix*, Table S4) showed that the Pt atoms in Pt SAC had a smaller coordination number (approximated to Pt-N_3) than that (approximated to Pt-N_4) in Pt-Au SAC; also, Pt-N_3 showed a shorter bonding length (1.88Å) than that of Pt-N_4 (2.01 Å), while the Au atoms in both Au SAC and Pt-Au SAC exhibited similar coordination parameters (approximated to Au-N_5). Notably, the lower coordination number and shorter bonding length of Pt atoms in Pt SAC indicated that it had a different locating position compared with that in Pt-Au SAC (*SI Appendix*, Figs. S11 and S12). Therefore, further microstructure analysis by considering the atomic structure of g-C_3N_4 was then performed.

When g-C_3N_4 was employed as the support, vacancies and sixfold cavities were two main pathways to stabilize single atoms (15, 16). In our case, to probe the structural features of SACs, electron paramagnetic resonance (EPR) spectroscopy was utilized. As shown in Fig. 2*D*, a characteristic band appeared at g = 2.0042, representative of C vacancies (as also confirmed by C/N mass ratio, X-ray photoelectron spectra (XPS) analysis and solid-state NMR spectra in *SI Appendix*, Table S3 and Figs. S13–S15). After only Pt atoms were loaded, the corresponding intensity reduced significantly, indicating decreased unpaired electrons and the coordinating of Pt with N atoms around C defective sites (17, 18). However, when Pt and Au were coloaded, this signal did not attenuate, showing nearly identical intensity with that of g-C_3N_4. This implied that Pt and Au atoms in 0.25% Pt-Au SAC did not coordinate with adjacent C/N atoms around C vacancies, thus causing no interference of unpaired electrons. The EPR signal of 0.25% Au SAC showed similar intensity with that of 0.25% Pt-Au SAC, suggesting that metal atoms in 0.25% Pt-Au SAC and 0.25% Au SAC were probably in the sixfold cavities of g-C_3N_4, instead of C vacancies. In comparison, Pt atoms in 0.25% Pt SAC were most likely existing in the C vacancies. Then, the mass ratio of $-NH_x$ (401eV) in N1s XPS was investigated to further probe the relationship between metal atoms and C vacancies (Fig. 2*E*)

(19, 20). When metal atoms occupied the C vacancies, the number of $-NH_x$ groups would decrease due to their substitution of H atoms. Results showed that $-NH_x$ mass ratios of 0.25% Pt-Au SAC and 0.25% Au SAC were 9.96 wt% and 10.03 wt%, respectively, which were close to that of pristine g-C_3N_4 (12.16 wt%). Nevertheless, the $-NH_x$ mass ratio of 0.25% Pt SAC dramatically decreased to 5.48 wt%. This was caused by the coordination between Pt atoms and NH_x groups around C vacancies, which was in good accordance with the result of EPR analysis (17, 18).

Based on the results above and combined with the optimization of density functional theory (DFT) calculations, the precise coordination structures of Pt SAC, Au SAC, and Pt-Au SAC were then drawn (Fig. 2*F* and *SI Appendix*, Fig. S16). Results showed that in the energy-favorable models, the coordination number of Au atoms (Au-N_5) in Au SAC and Pt-Au SAC was identical. In contrast, the coordination structures of Pt atoms in Pt SAC and Pt-Au SAC were Pt-N_3 and Pt-N_4, respectively, which was in good agreement with our EXAFS fitting results. Also, unlike the Pt atoms in heptazine cavities over Pt-Au SAC, the Pt atoms in Pt SAC were located in C vacancies, which is consistent with those of the EPR and XPS analysis (Fig. 2 *D* and *E*).

Solar Water Splitting over Binary Single Sites. Then, solar water splitting was performed to compare the reactivities of as-prepared binary and single metal–site catalysts (Fig. 3). Enhanced catalytic performance was observed in all loading contents, especially obvious in loading content of 0.25 wt%; thus, 0.25% Pt-Au SAC (where the mass ratio of Pt/Au is around 1:1) was selected as the model to illustrate the promotional interaction between Pt and Au binary sites (Fig. 3*A* and *SI Appendix*, Figs. S17 and S18 and Tables S5–S7). The catalytic performance of 0.25% Pt-Au SAC (1.88 mmol g^{-1} h^{-1}, apparent quantum efficiency of 1.72% at 365 nm) reached 4.9 and 2.3 times over those of 0.25% Pt SAC and 0.25% Au SAC, respectively. Because variation of the Pt/Au mass ratio in 0.25% Pt-Au SAC can also affect catalytic performance, the effect of the Pt/Au mass ratio on catalytic activities was also investigated (*SI Appendix*, Fig. S18). The best catalytic performance was obtained when the Pt/Au mass ratio was 1:1, which could be attributed to the formation of the most abundant Pt-Au binary single sites. Therefore, unless otherwise specified, 0.25% Pt-Au SAC in this work refers to the sample with total metal loading 0.25 wt%, and the mass proportion of Pt/Au was 1:1. The cycle test result showed that 91% of the reactivity was maintained after three cycles, indicating that the binary sites were relatively stable (Fig. 3*B*), which is further confirmed by XRD patterns and HAADF-STEM analysis of samples after reaction (*SI Appendix*, Figs. S19 and S20). Then, to identify the origin of the enhancement, a series of samples were designed and evaluated (Fig. 3*C*). It is shown that the activities of both 0.12% Pt SAC (0.26 mmol g^{-1} h^{-1}) and 0.12% Au SAC (0.42 mmol g^{-1} h^{-1}) were weak, with a combined hydrogen evolution rate of 0.68 mmol g^{-1} h^{-1}, which is only 36.2% over 0.25% Pt-Au SAC (1.88 mmol g^{-1} h^{-1}). This result showed that the activity enhancement was mainly attributed to the coexistence and synergism of Pt and Au binary sites. The influence of sacrificial agents on solar water splitting was also assessed. When ascorbic acid was employed as the sacrificial agent, the highest reactivity was obtained. The interaction between sacrificial agents and binary sites SACs would be discussed in our following work.

Analysis of the Enhancing Effect of Localized Dipoles. Thereafter, the significant activity enhancement of binary sites inspired us to further investigate its working mechanism. Generally, the activity of photocatalysts was highly correlated with their electronic states and band structures, which determine the

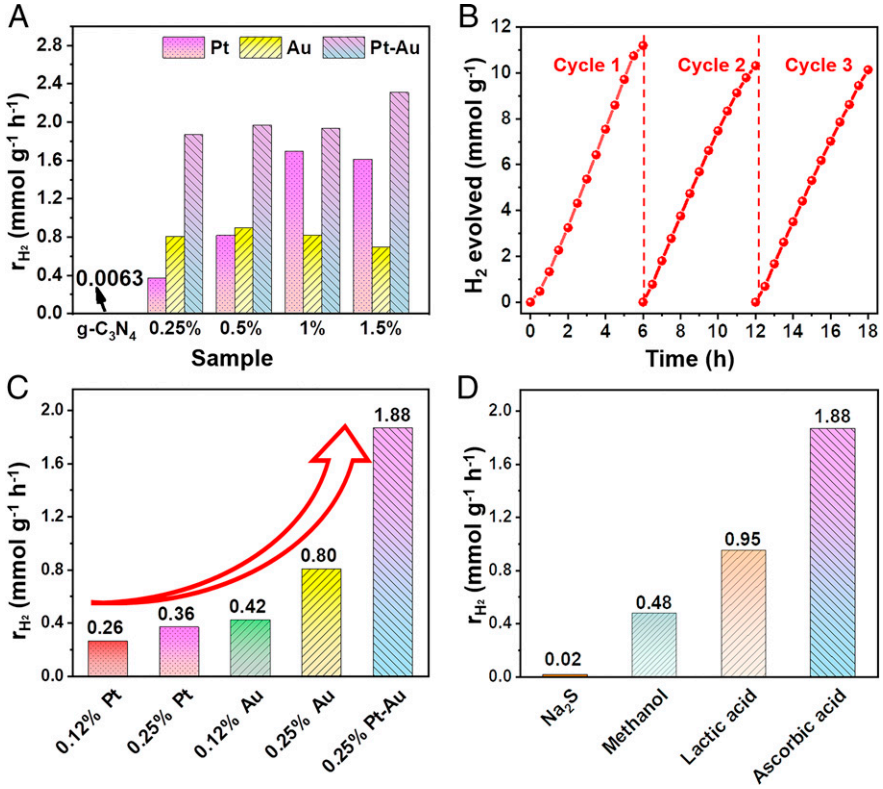

Fig. 3. Solar water splitting over binary single sites. (*A*) Solar water splitting evaluation of as-prepared SACs. (*B*) Cycle test of 0.25% Pt-Au SAC. (*C*) Comparison of different samples under loading contents 0.12% and 0.25%. (*D*) The influence of sacrificial agents on solar water splitting.

efficiency of charge separation and transfer (21). Band alignments of as-prepared SACs were measured using UV-visible (UV-vis) diffuse reflectance spectra and valence band XPS (*SI Appendix*, Figs. S21–S23), where Pt SAC, Au SAC, and Pt-Au SAC had similar alignments; thus, the major contribution of band structures can be ruled out. In this case, the different metal species in Pt-Au SAC reminded us of the charge imbalance between adjacent Pt and Au sites. Thus, the theoretical simulations were carried out to display the electronic states of adjacent Pt and Au sites (Fig. 4*A*). Results showed that Bader charges of adjacent Pt and Au atoms are −0.38 and −0.48 e, respectively, indicating the unbalanced charge distribution zones in Pt-Au SAC (the molecular fragments in the image Fig. 4*A*). In comparison, the charge imbalance in Pt SAC and Au SAC was weaker, especially in Pt SAC, which showed the almost symmetric charge distribution. This suggested the formation of stronger localized molecular dipoles over Pt-Au SAC than those of unary counterparts. A typical dipole can be approximated by a pair of positive and negative charges of equal magnitude separated by a small distance (Fig. 4*B*), which are universal in chemical molecules, due to the uneven distribution of charge centers. In this study, bond dipoles were formed in Pt-N and Au-N bonds because of the different electronegativities between precious metals and N atoms (Fig. 4*B*). The vector superposition of bond dipoles would then form molecular dipoles in the adjacent zones of single metal sites. Thereafter, we performed molecular dipole moment calculations (Fig. 4*C*), and results showed that the molecular dipole moment of binary sites catalyst Pt-Au SAC (6.16 D) was larger than those of Pt SAC (2.15 D) and Au SAC (5.73 D). And all these dipole moments showed directions parallel to the surface of g-C_3N_4 nanosheet support. Moreover, the molecular fragments in Fig. 4*C* constituted the whole photocatalyst; therefore, in Pt-Au SAC, the superposition of the enhanced molecular dipole moments would partially contribute to the enhancement of the whole internal electric field, which can boost the charge separation and transfer during the photocatalysis process (22).

To verify the enhancement of internal electric field in Pt-Au SAC, several tests, including Kelvin probe force microscopy, were then performed (Fig. 4*D* and *SI Appendix*, Figs. S24–S26 and Tables S8 and S9). The strength of internal electric field could be obtained by calculating the surface potential and the

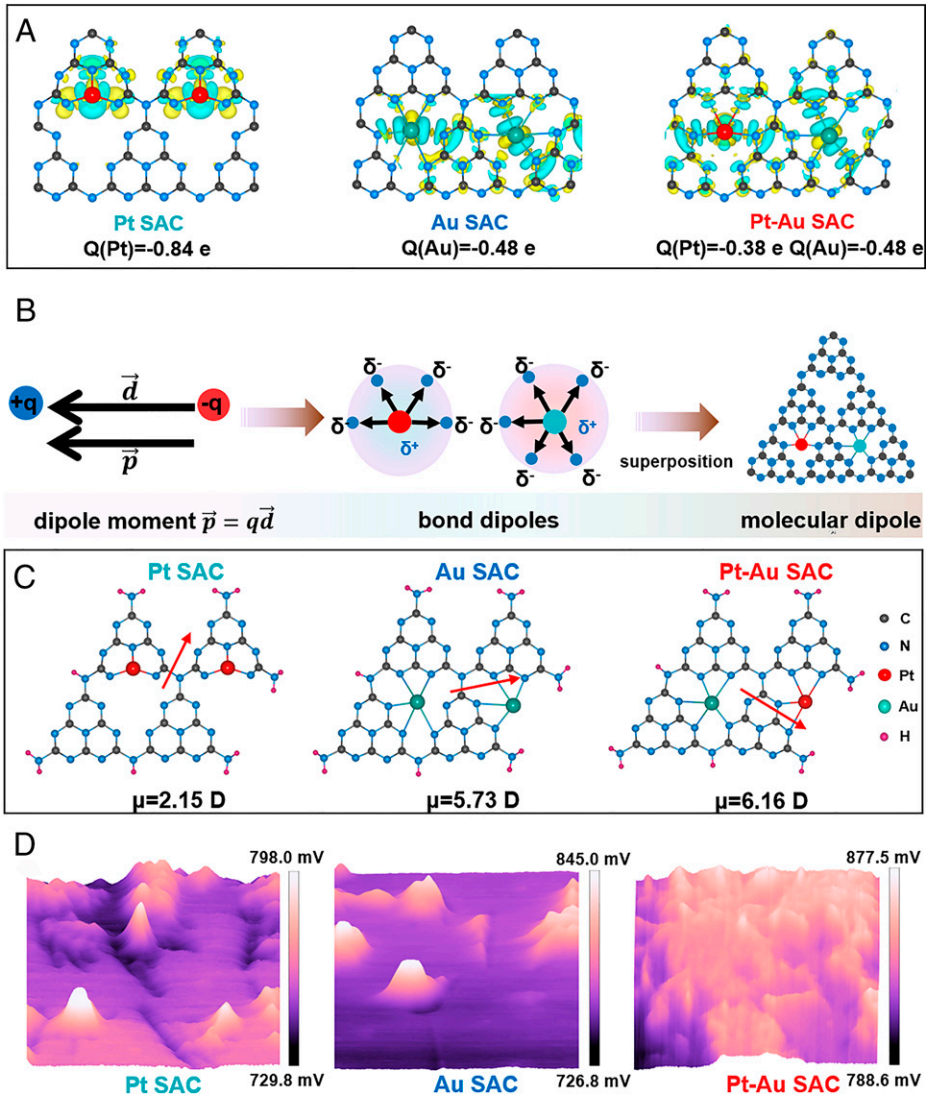

Fig. 4. Analysis of the enhancing effect of localized dipoles. (*A*) Calculated charge distribution over metal sites of as-prepared SACs where yellow and light blue iso-surfaces represent charge accumulation and depletion, respectively. (*B*) Illustration of a typical electric dipole and bond dipoles in Pt-Au SAC. (*C*) The calculated molecular dipole moments of Pt SAC, Au SAC, and Pt-Au SAC, respectively, where the red arrows represent the direction of the dipole moments (unit of dipole moment: Debye). (*D*) The KPFM images of as-prepared SACs. The size of the selected areas was 10 μm × 10 μm.

surface charge density of catalysts, where the surface potential could be acquired by KPFM and the surface charge density could be obtained by zeta potential measurements (23, 24).

The relationship between surface potential, surface charge density, and internal electric field of a semiconductor is expressed as follows (25–27):

$$E = \left(\frac{-2V_s\rho}{\varepsilon\varepsilon_0}\right)^{1/2}, \quad [1]$$

where E is the strength of internal electric field (in V/m), V_s is the surface potential (in V), ρ is the surface charge density (in C/m^2), ε is the low-frequency dielectric constant, and ε_0 is the vacuum dielectric constant, 8.854×10^{-12} F/m.

As we can see in the above equation, the strength of internal electric field was proportional to 0.5 power of both the surface potential and the surface charge density. Then the strength of the internal electric field could be evaluated by the combination of those two parameters. As exhibited in Fig. 4*D* of the KPFM images, Pt-Au SAC shows higher surface potential (average surface potential 827.0 mV) than those of both Pt SAC and Au SAC (average surface potential 753.3 mV and 783.7 mV, respectively, *SI Appendix*, Table S8). In addition, those three SACs have similar zeta potentials (*SI Appendix*, Table S9). Thus, the difference in internal electric fields for SACs here can be considered as mainly proportional to 0.5 power of the surface potential. The higher surface potential of Pt-Au SAC indicates its stronger internal electric field, which was consistent with the molecular dipole moment calculations. Generally, a stronger internal electric field could vastly improve the separation efficiency of photo-induced carriers and enhance the catalytic reactivity (28, 29).

Enhanced Charge Transportation Dynamics. Thereafter, TA was employed to investigate the charge transport dynamics of as-prepared SACs (Fig. 5 *A* and *B* and *SI Appendix*, Figs. S27–S31). The pump pulse with center wavelength 330 nm was chosen to effectively excite the as-prepared samples (as shown in *SI Appendix*, Fig. S21*A*). Results showed that all samples had similar charge transportation dynamics where broad positive absorption features between 600 and 770 nm were observed, which is due to the excited-state absorption that reflects the lifetime of photoexcited electrons in semiconductors (30). Negative profiles were obtained between 460 and 520 nm, which were attributed to probe bleach of the neutral ground-state absorption caused by neutral singlet excitons (31). Since dynamics observed in the range 460–520 nm involved the contribution of both holes and electrons, the relaxation process could be better described using a positively valued absorption region of 600–770 nm. A set of representative data taken at 760 nm were investigated. Results showed that TA spectra over all as-prepared samples featured an instantaneous buildup of TA signal, followed by a relaxation process in a biexponential manner. The relaxation process consists of two steps: the time constant τ_1 is the process of energized electrons captured by near-band-gap states, and the much slower time constant τ_2 was attributed to the recombination of trapped electrons and valence band holes (32, 33). The fitting results are as follows: $\tau_1 = 6.39 \pm 0.99$ ps (61%), $\tau_2 = 370.1 \pm 20.8$ ps (39%) for-pristine g-C_3N_4, $\tau_1 = 4.45 \pm 0.63$ ps (59%) and $\tau_2 = 246.5 \pm 52.1$ ps (41%) for Pt SAC, $\tau_1 = 3.54 \pm 0.55$ ps (61%) and $\tau_2 = 201.4 \pm 49.3$ ps (39%) for Au SAC, $\tau_1 = 2.04 \pm 0.62$ ps (64%) and $\tau_2 = 124.8 \pm 20.4$ ps (36%) for Pt-Au SAC. The average lifetimes were calculated to be 360.10, 240.19, 196.03, 121.37 ps for g-C_3N_4, Pt SAC, Au SAC and Pt-Au SAC, respectively. The almost three-fold decrease of the average lifetime over Pt-Au SAC compared with pristine g-C_3N_4 could be ascribed to the opening of additional channels for electron transfer (34). Besides, the accelerated time constant τ_1 (2.04 ps) over Pt-Au SAC also proved the efficient electron transfer over Pt-Au binary single sites. The same conclusion could be drawn from the time-resolved photoluminescence (PL) spectra measurements (*SI Appendix*, Figs. S32 and S33 and Tables S10 and S11), indicating that the coexistence of Pt and Au atomic sites boosted the electron transfer and trapping process from the conduction band, which enhanced the separation of photo-induced charges and promoted the photocatalytic process.

To further confirm the enhanced charge transportation process due to the strengthened internal electric field in Pt-Au SAC, the steady-state surface photovoltage (SS-SPV), electrochemical impedance spectroscopy (EIS), PL spectra, and transient photocurrent curve (TPC) measurements were then performed (Fig. 5 *C*–*F*). The SS-SPV spectra could directly evaluate the intensity of the internal electric field caused by the charge separation process. Results displayed an obvious surface photovoltage response in the range of 300–420 nm, where Pt-Au SAC showed the highest photovoltage signal, indicating the highest charge separation and transfer efficiency (Fig. 5*C*). Meanwhile, PL spectra of as-prepared samples were collected under the excitation of 330 nm (which could effectively excite all the samples as shown in *SI Appendix*, Fig. S21*A*) using identical testing conditions. Due to the basically same absorbances of as-prepared samples, the obtained results could be employed to discuss the charge separation/transfer efficiency. The quenched signal caused by the radiative recombination between photoexcited electrons and holes in PL spectra showed that 0.25% Pt-Au SAC had the highest charge separation efficiency due to the faster electron transfer process (Fig. 5*D*). This is self-consistent with the above TA analysis. As shown by EIS (Fig. 5*E*), the arc radius of 0.25% Pt-Au SAC was the smallest among all SACs, indicating the smallest charge transfer resistance under photocatalytic conditions. The simulated interfacial charge transfer resistance of Pt-Au SAC was 117 kΩ, which is much smaller than that of Pt SAC, Au SAC, and g-C_3N_4 (228, 175, and 285 kΩ, respectively). Besides, the TPC results showed that 0.25% Pt-Au SAC had considerably higher photocurrent than 0.25% Au SAC, 0.25% Pt SAC, and g-C_3N_4 (Fig. 5*F*). This demonstrated that binary sites Pt and Au could significantly improve the separation efficiency of photo-induced carriers, thus enhancing photocatalytic activity.

Moreover, the reaction barrier was also evaluated over as-prepared SACs (*SI Appendix*, Figs. S34–S36), which is another essential factor that should be considered in solar water splitting. Results showed the H* adsorption free energy over Pt-Au SAC was only −0.09 eV, which is closer to 0 (the ideal energy level) than Pt SAC (−0.40 eV) and Au SAC (−0.37 eV). This indicated an optimized energy barrier in Pt-Au binary single sites, which is favorable for the hydrogen evolution process. In addition, the calculation results (*SI Appendix*, Fig. S36) of H* adsorption free energy revealed that both Pt and Au single atoms in Pt-Au SAC could function as the H* reduction sites. However, the stronger adsorption of H* on the Au site (−0.73 eV) compared with the Pt counterpart (−0.09 eV) indicated that the Pt atomic sites were more favorable for the hydrogen generation process. This was also consistent with the calculated charge distribution (Fig. 4*A*) results showing that less charge distribution was observed around Pt atomic sites (Bader charges of adjacent Pt and Au atoms are −0.38 and −0.48 e, respectively).

Discussion

In summary, a binary single-site catalyst composed of a precious metal (Pt) and another precious metal (Au) was explored. Promotional interaction between binary sites was observed in solar water splitting, where the activity of the Pt-Au binary sites

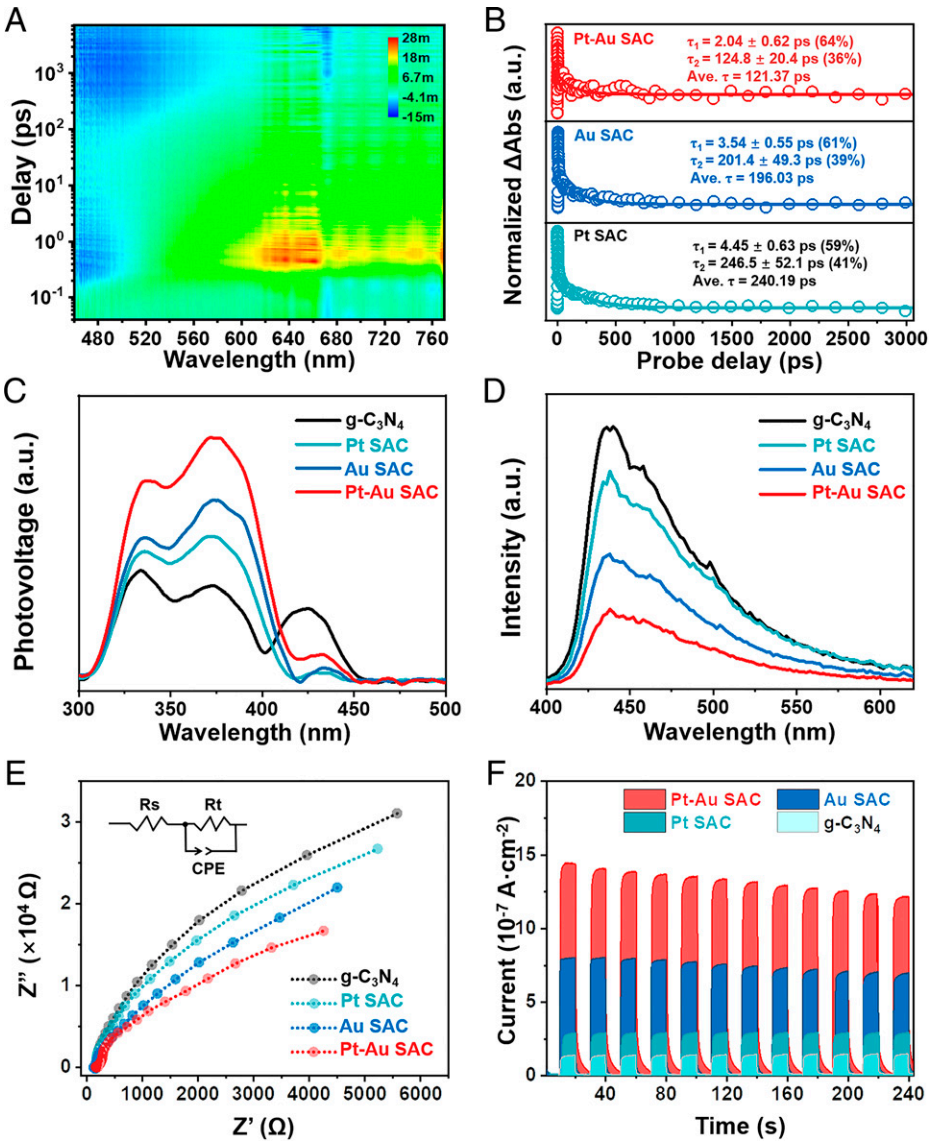

Fig. 5. Enhanced charge transportation dynamics. (*A*) Contour plot of the TA spectrum over 0.25% Pt-Au SAC tested in ethylene glycol and excited by a 330-nm pump. (*B*) TA kinetics probed at 760 nm for as-prepared SACs. (*C*) SS-SPV responses of as-prepared catalysts. (*D*) PL spectra of as-prepared catalysts. (*E*) TPC responses of as-prepared catalysts. (*F*) EIS of as-prepared catalysts.

(Pt-Au SAC) reached 1.88 mmol g^{-1} h^{-1} (apparent quantum efficiency of 1.72% at 365 nm), 4.9 times and 2.3 times as those over Pt SAC and Au SAC, respectively. Theoretical and spectroscopic results showed that Pt and Au atoms in Pt-Au SAC and Au SAC were preferentially stabilized in sixfold cavities between heptazine subunits (with Pt-N_4/Au-N_5 coordination). However, the Pt atoms in Pt SAC were prone to occupy C vacancies (with Pt-N_3 coordination). The larger charge imbalance in the zone of adjacent Pt and Au sites of Pt-Au SAC led to the enhancement of localized molecular dipoles compared with those in unary counterparts, greatly improving the charge separation and transfer by strengthening the internal electric field and thus boosting the solar water splitting. Besides, the lowest reaction barrier was also realized on the Pt-Au binary sites, also contributing to solar water splitting.

Materials and Methods

Preparation of Catalysts. All chemicals are of analytical grade and were used directly as received without further purification. g-C_3N_4 was prepared by a modified heat-etching method using the mixture of urea and thiourea (1% wt of thiourea to urea) as the precursor (35). Then, the obtained material was reduced at 500 °C in the atmosphere of H_2/Ar (5 vol% H_2/95 vol% Ar) for 1 h. Pt SAC, Au SAC, and Pt-Au SAC were prepared by a simple impregnation-adsorption method (36). In a typical procedure, briefly, 200 mg g-C_3N_4 was dispersed in 50 mL distilled water, and then appropriate amounts of $H_2PtCl_6{\cdot}6H_2O$ (1.48 mg_{Pt} mL^{-1}) and $HAuCl_4$ (2 mg_{Au} mL^{-1}) solutions were added dropwise, followed by stirring at 70 °C for 2 h. The product was obtained by filtration, repeated washing with deionized water and ethanol, and vacuum drying at 60 °C overnight.

Characterization. XRD patterns were collected using a Rigaku D/Max 2200PC X-ray diffractometer with Cu Kα radiation (λ = 0.15418 nm). High-resolution transmission electron microscopy (HR-TEM) analyses were performed using a JEOL JEM-2100F at an accelerating voltage of 200 kV (Japan). The HAADF images and elemental mapping results were acquired using the STEM mode of FEI Titan Themis G1 with double aberration correctors and four energy dispersive spectrometer (EDS) detectors, each of which had an active area of 30 mm^2 for detecting the EDS signals. Thermal analysis was conducted via a synchronous thermal analyzer (Mettler Toledo, TGA DSC1). Fourier transform infrared spectra were obtained on an infrared spectrometer (Bruker tensor 27, German). Metal loading contents were determined by ICP-MS (X7 Series, Thermo Electron Corporation). XPS measurements were carried out in a

Thermal ESCALAB 250 electron spectrometer using Al Kα radiation X-ray source (hν = 1,486.6 eV). Solid-state ^{13}C and ^{1}H NMR spectra were recorded by a Bruker Avance III WB 400 at 10KHz resonance frequency. UV-vis diffused reflectance spectra of the samples were obtained using a Shimadzu Corporation UV-vis spectrophotometer to record the absorption spectra of the samples. Kelvin probe force microscopy images were obtained by using a Bruker's Dimension Icon Atomic Force Microscope System in lift mode. Zeta potentials were measured with a Zetasizer Nano ZS90 (Malvern Instruments). PL spectra were measured using an Edinburgh Instruments FLS920P equipped with a Xe lamp-920 at room temperature under the excitation of 330 nm. Time-resolved PL decay curves were recorded on a FLS920 fluorescence lifetime spectrophotometer under the excitation of 330 nm and probed at 440 nm. The femtosecond-TA measurements were carried out on a Helios pump−probe system (Ultrafast Systems). White-light continuum probe pulses (350 − 800 nm) were produced by focusing a miniscule portion of the fundamental 800-nm laser pulses (Coherent, 800 nm, 1 kHz, 7 mJ $pulse^{-1}$, 35 fs) onto a calcium fluoride crystal. Pump pulses centered at 330 nm were generated from an optical parametric amplifier (TOPAS-800 fs), and the samples were measured by probing polarizations oriented at the magic angle. The instrument response function was determined as ∼100 fs by a routine cross-correlation procedure. The SPV spectra were obtained on a CEL-SPS1000 surface photovoltage spectrometer, a product of Beijing CEAULIGHT. The measurement systems included a lock-in amplifier (SR830, Stanford Research Systems) and a simple chamber. Electron spin resonance (EPR) spectroscopy was conducted on a Bruker model EPR JES-FA200 spectrometer. Photoelectrochemical activity tests were performed using an electrochemical work station (CHI660E Instruments) with a standard three-electrode system (an Ag/AgCl electrode reference electrode and a Pt foil counter electrode); 0.5 M Na_2SO_4 solution was used as the electrolyte.

X-Ray Absorption Fine Structure. The X-ray absorption fine structure spectra (Pt and Au L_3-edge) were collected at 1W1B station in Beijing Synchrotron Radiation Facility (BSRF). The storage rings of BSRF were operated at 2.5 GeV with a maximum current of 250 mA. Using an Si (111) double-crystal monochromator, data collection was carried out in transmission mode using an ionization chamber. All spectra were collected in ambient conditions. The acquired EXAFS data were processed according to the standard procedures using the ATHENA module implemented in the IFEFFIT software packages (37). The k_3-weighted EXAFS spectra were obtained by subtracting the post-edge background from the overall absorption and then normalizing with respect to the edge-jump step. Subsequently, k_3-weighted χ(k) data of Pt and Au K-edge were Fourier transformed to real (R) space using Hanning windows (dk = 1.0 $Å^{-1}$) to separate the EXAFS contributions from different coordination shells. To obtain the quantitative structural parameters around central atoms, least-squares curve parameter fitting was performed using the ARTEMIS module of IFEFFIT software packages.

Theoretical Calculation. All the calculations were carried out based on DFT with the Perdew–Burke–Ernzerbof form of generalized gradient approximation functional by employing the Vienna ab initio simulation package (VASP) (38–41). The Blöchl's all-electron-like projector augmented wave method was used to describe the interactions between valence electrons and ion cores (42, 43). The wave functions at each k-point were expanded with a plane wave basis set, and a kinetic cutoff energy of 450 eV was applied. Brillouin zone integration was approximated by a sum over special selected k-points using the gamma-centered Monkhorst–Pack grid, which was set to 3 × 3 × 1 (44). The electron occupancies were determined according to Fermi scheme with an energy smearing of 0.1 eV. Geometries were optimized until the energy was converged to 1.0×10^{-6} eV/atom and the force was converged to 0.01 eV/Å. To avoid periodic interactions for all the structures, a vacuum layer as large as 20 Å is used along the c direction normal to the surface. The adsorption energies (E_{ads}) of Pt and Au atom on perfect and defective g-C_3N_4 were calculated using the following formula:

$$E_{ads} = \frac{E_{sub+Pt+Au} - E_{sub} - E_{Pt} - E_{Au}}{2}. \quad [2]$$

The molecular dipole moment computations were carried out by the Gaussian 16 program Revision B01. The theoretical method was the popular B3LYP, adding the D3 version of Grimme's dispersion with Becke–Johnson damping function (45–48). The triple-zeta turbomole basis set, Def2-TZVP, was used for C, H, N, Au, and Pt atoms (49). The effective core potential included in the Def2-TZVP basis set was used for Au and Pt atoms to reduce the computational cost. We choose the fragment of the whole unit cell of three types of crystal structures to calculate the dipole moment. The edge atoms of the fragments are saturated with hydrogen atoms. The fragment we choose is in the unit cell for three crystal structures.

Catalytic Performance Evaluation. The photocatalytic hydrogen production test was performed with a photocatalytic activity evaluation system (Beijing CEAULIGHT, product model CEL-PAEM-D8). A 300-W Xe lamp was employed as the light source, and the area of the surface irradiated was about 31 cm^2. A 50-mg sample was dispersed in 100 mL aqueous solution containing 20 vol% 0.75 M ascorbic acid as sacrificial agent. The suspension was illuminated under continuous magnetic stirring after being thoroughly degassed by evacuation under 283 K. Automatic sampling procedure was set to record H_2 production amount in 6 h.

The apparent quantum efficiency (AQE) at a wavelength of 365 nm was measured under the identical reaction condition by placing band-pass filters in front of the light source. The CEL-NP2000 spectroradiometer was used to measure the intensity of the incident light. The AQE was calculated according to the following equation (50):

$$\begin{aligned} \mathrm{AQE}[\%] &= \frac{\text{number of reacted electrons}}{\text{number of incident photons}} \times 100 \\ &= \frac{\text{number of evolved } H_2 \text{ molecules} \times 2}{\text{number of incident photons}} \times 100. \end{aligned} \quad [3]$$

Data Availability. All study data are included in the article and/or *SI Appendix*.

ACKNOWLEDGMENTS. This work was supported by the National Natural Science Foundation of China (Grant Nos. 22076082, 22170280, and 22121004), the Program of Introducing Talents of Discipline to Universities (Grant No. BP0618007), and the Frontiers Science Center for New Organic Matter (Grant No. 63181206).

1. J. D. Smith *et al.*, Organopolymer with dual chromophores and fast charge-transfer properties for sustainable photocatalysis. *Nat. Commun.* **10**, 1–16 (2019).
2. Z. B. Fang *et al.*, Boosting interfacial charge-transfer kinetics for efficient overall CO_2 photoreduction via rational design of coordination spheres on metal-organic frameworks. *J. Am. Chem. Soc.* **142**, 12515–12523 (2020).
3. T. Takata *et al.*, Photocatalytic water splitting with a quantum efficiency of almost unity. *Nature* **581**, 411–414 (2020).
4. R. T. Chen *et al.*, Charge separation via asymmetric illumination in photocatalytic Cu_2O particles. *Nat. Energy* **3**, 655–663 (2018).
5. B. Qiao *et al.*, Single-atom catalysis of CO oxidation using Pt_1/FeO_x. *Nat. Chem.* **3**, 634–641 (2011).
6. P. Liu *et al.*, Photochemical route for synthesizing atomically dispersed palladium catalysts. *Science* **352**, 797–801 (2016).
7. X. Zheng *et al.*, Origin of enhanced water oxidation activity in an iridium single atom anchored on NiFe oxyhydroxide catalyst. *Proc. Natl. Acad. Sci. U.S.A.* **118**, 1–7 (2021).
8. H. Zou, W. Rong, S. Wei, Y. Ji, L. Duan, Regulating kinetics and thermodynamics of electrochemical nitrogen reduction with metal single-atom catalysts in a pressurized electrolyser. *Proc. Natl. Acad. Sci. U.S.A.* **117**, 29462–29468 (2020).
9. L. Yang *et al.*, Unveiling the high-activity origin of single-atom iron catalysts for oxygen reduction reaction. *Proc. Natl. Acad. Sci. U.S.A.* **115**, 6626–6631 (2018).
10. Y. Cao *et al.*, Atomic-level insight into optimizing the hydrogen evolution pathway over a Co_1-N_4 single-site photocatalyst. *Angew. Chem. Int. Ed. Engl.* **56**, 12191–12196 (2017).
11. X. Wu *et al.*, Surface step decoration of isolated atom as electron pumping: Atomic-level insights into visible-light hydrogen evolution. *Nano Energy* **45**, 109–117 (2018).
12. J. Wang *et al.*, Design of N-coordinated dual-metal sites: A stable and active Pt-free catalyst for acidic oxygen reduction reaction. *J. Am. Chem. Soc.* **139**, 17281–17284 (2017).
13. W. Ren *et al.*, Isolated diatomic Ni-Fe metal-nitrogen sites for synergistic electroreduction of CO_2. *Angew. Chem. Int. Ed. Engl.* **58**, 6972–6976 (2019).
14. Y. Tang *et al.*, Synergy of single-atom Ni_1 and Ru_1 sites on CeO_2 for dry reforming of CH_4. *J. Am. Chem. Soc.* **141**, 7283–7293 (2019).
15. G. Vilé *et al.*, A stable single-site palladium catalyst for hydrogenations. *Angew. Chem. Int. Ed. Engl.* **54**, 11265–11269 (2015).
16. Z. P. Chen *et al.*, Stabilization of single metal atoms on graphitic carbon nitride. *Adv. Funct. Mater.* **27**, 1605785 (2017).
17. J. Wan *et al.*, Defect effects on TiO_2 nanosheets: Stabilizing single atomic site Au and promoting catalytic properties. *Adv. Mater.* **30**, 1705369 (2018).
18. Y. Chen *et al.*, Engineering the atomic interface with single platinum atoms for enhanced photocatalytic hydrogen production. *Angew. Chem. Int. Ed. Engl.* **59**, 1295–1301 (2020).
19. S. Cao *et al.*, Sulfur-doped g-C_3N_4 nanosheets with carbon vacancies: General synthesis and improved activity for simulated solar-light photocatalytic nitrogen fixation. *Chem. Eng. J.* **353**, 147–156 (2018).
20. S. N. Li *et al.*, Effective photocatalytic H_2O_2 production under visible light irradiation at g-C_3N_4 modulated by carbon vacancies. *Appl. Catal. B* **190**, 26–35 (2016).

21. J. H. Clark *et al.*, Visible light photo-oxidation of model pollutants using $CaCu_3Ti_4O_{12}$: An experimental and theoretical study of optical properties, electronic structure, and selectivity. *J. Am. Chem. Soc.* **133**, 1016–1032 (2011).
22. Y. Guo, W. Shi, Y. Zhu, Internal electric field engineering for steering photogenerated charge separation and enhancing photoactivity. *EcoMat* **1**, 12007 (2019).
23. R. Chen, F. Fan, T. Dittrich, C. Li, Imaging photogenerated charge carriers on surfaces and interfaces of photocatalysts with surface photovoltage microscopy. *Chem. Soc. Rev.* **47**, 8238–8262 (2018).
24. J. Zhu *et al.*, Direct imaging of highly anisotropic photogenerated charge separations on different facets of a single $BiVO_4$ photocatalyst. *Angew. Chem. Int. Ed. Engl.* **54**, 9111–9114 (2015).
25. J. S. Im *et al.*, Reduction of oscillator strength due to piezoelectric fields in $GaN/Al_xGa_{1-x}N$ quantum wells. *Phys. Rev. B Condens. Matter Mater. Phys.* **57**, R9435 (1998).
26. P. Lefebvre *et al.*, Time-resolved photoluminescence as a probe of internal electric fields in GaN-(GaAl)N quantum wells. *Phys. Rev. B Condens. Matter Mater. Phys.* **59**, 15363–15367 (1999).
27. G. Morello *et al.*, Intrinsic optical nonlinearity in colloidal seeded grown CdSe/CdS nanostructures: Photoinduced screening of the internal electric field. *Phys. Rev. B Condens. Matter Mater. Phys.* **78**, 195313 (2008).
28. J. Li, L. Cai, J. Shang, Y. Yu, L. Zhang, Giant enhancement of internal electric field boosting bulk charge separation for photocatalysis. *Adv. Mater.* **28**, 4059–4064 (2016).
29. Y. Guo, W. X. Shi, Y. F. Zhu, Y. P. Xu, F. Y. Cui, Enhanced photoactivity and oxidizing ability simultaneously via internal electric field and valence band position by crystal structure of bismuth oxyiodide. *Appl. Catal. B* **262**, 118262 (2020).
30. L. Wang *et al.*, Designing p-type semiconductor-metal hybrid structures for improved photocatalysis. *Angew. Chem. Int. Ed. Engl.* **53**, 5107–5111 (2014).
31. Z. Chen, Q. Zhang, Y. Luo, Experimental identification of ultrafast reverse hole transfer at the interface of the photoexcited methanol/graphitic carbon nitride system. *Angew. Chem. Int. Ed. Engl.* **57**, 5320–5324 (2018).
32. X. Jiao *et al.*, Defect-mediated electron-hole separation in one-unit-cell $ZnIn_2S_4$ layers for boosted solar-driven CO_2 reduction. *J. Am. Chem. Soc.* **139**, 7586–7594 (2017).
33. H. Huang *et al.*, Unraveling surface plasmon decay in core-shell nanostructures toward broadband light-driven catalytic organic synthesis. *J. Am. Chem. Soc.* **138**, 6822–6828 (2016).
34. X. Ma, L. Wang, Q. Zhang, H. L. Jiang, Switching on the photocatalysis of metal-organic frameworks by engineering structural defects. *Angew. Chem. Int. Ed. Engl.* **58**, 12175–12179 (2019).
35. S. W. Cao *et al.*, Single-atom engineering of directional charge transfer channels and active sites for photocatalytic hydrogen evolution. *Adv. Funct. Mater.* **28**, 1802169 (2018).
36. Z. Zhang *et al.*, The simplest construction of single-site catalysts by the synergism of micropore trapping and nitrogen anchoring. *Nat. Commun.* **10**, 1–7 (2019).
37. B. Ravel, M. Newville, ATHENA, ARTEMIS, HEPHAESTUS: Data analysis for X-ray absorption spectroscopy using IFEFFIT. *J. Synchrotron Radiat.* **12**, 537–541 (2005).
38. J. P. Perdew, K. Burke, M. Ernzerhof, Generalized gradient approximation made simple. *Phys. Rev. Lett.* **77**, 3865–3868 (1996).
39. G. Kresse, J. Furthmüller, Efficiency of ab-initio total energy calculations for metals and semiconductors using a plane-wave basis set. *Comput. Mater. Sci.* **6**, 15–50 (1996).
40. G. Kresse, J. Hafner, Ab initio molecular dynamics for liquid metals. *Phys. Rev. B Condens. Matter* **47**, 558–561 (1993).
41. G. Kresse, J. Hafner, Ab initio molecular-dynamics simulation of the liquid-metal-amorphous-semiconductor transition in germanium. *Phys. Rev. B Condens. Matter* **49**, 14251–14269 (1994).
42. P. E. Blöchl, Projector augmented-wave method. *Phys. Rev. B Condens. Matter* **50**, 17953–17979 (1994).
43. G. Kresse, D. Joubert, From ultrasoft pseudopotentials to the projector augmented-wave method. *Phys. Rev. B Condens. Matter Mater. Phys.* **59**, 1758–1775 (1999).
44. H. J. Monkhorst, J. D. Pack, Special points for brillouin-zone integrations. *Phys. Rev. B* **13**, 5188–5192 (1976).
45. A. D. Becke, Density-functional exchange-energy approximation with correct asymptotic behavior. *Phys. Rev. A Gen. Phys.* **38**, 3098–3100 (1988).
46. A. D. Beck, Density-functional thermochemistry. III. The role of exact exchange. *J. Chem. Phys.* **98**, 5648 (1993).
47. S. Grimme, S. Ehrlich, L. Goerigk, Effect of the damping function in dispersion corrected density functional theory. *J. Comput. Chem.* **32**, 1456–1465 (2011).
48. C. Lee, W. Yang, R. G. Parr, Development of the Colle-Salvetti correlation-energy formula into a functional of the electron density. *Phys. Rev. B Condens. Matter* **37**, 785–789 (1988).
49. F. Weigend, R. Ahlrichs, Balanced basis sets of split valence, triple zeta valence and quadruple zeta valence quality for H to Rn: Design and assessment of accuracy. *Phys. Chem. Chem. Phys.* **7**, 3297–3305 (2005).
50. M. Liu, D. Jing, Z. Zhou, L. Guo, Twin-induced one-dimensional homojunctions yield high quantum efficiency for solar hydrogen generation. *Nat. Commun.* **4**, 1–8 (2013).